

A Method to Quantify the Collective Impact of Grain Boundaries on the Internal Quantum Efficiency of Multicrystalline Silicon Solar Cells

Aleo Paolo Pacho* and Markus Rinio

Herein, a method to quantify the amount of reduction in the internal quantum efficiency (IQE) of multicrystalline silicon solar cells that can be attributed to grain boundaries is presented. By correlating the IQE maps obtained via light beam induced current (LBIC) topography with optical images of Secco-etched samples, the distribution of IQE values at the positions of grain boundaries can be compared with the distribution of IQE values for all other positions where other defects may exist. The segmentation of IQE at 826 nm maps of the samples shows grain boundaries to be more detrimental compared with the combined effects of all other defects that may exist in other regions of the cell. The grain boundaries reduce the average IQE by up to 4.07% absolute for the cell from the bottom of the ingot.

quantum efficiency (IQE) at the given wavelength. Furthermore, it has been demonstrated that the recombination activity of dislocations can be quantified from the IQE maps.^[9–13] For grain boundaries, the approach is typically based on the contrast profile of individual grain boundaries, i.e., the linescan contrast between the current induced by either an electron beam or a light beam at the grain boundary and the background current value.^[14–20] Although such an approach is extremely useful in understanding the behavior of individual grain boundaries, it may be difficult to obtain an overall assessment of the impact


1. Introduction

Multicrystalline silicon (mc-Si) grown via directional solidification continues to be one of the most widely used raw materials in the solar cell market. This is because this material strikes a delicate balance between conversion efficiency and cost of production, consuming about five times less energy per kilogram during ingot growth compared with monocrystalline silicon ingot.^[1] Extended crystal defects, particularly grain boundaries, are inherent in this type of material and are regarded as a major factor affecting its efficiency. Extensive efforts have therefore been made to study their impact on the performance of the solar cell.^[2–8] Topographic characterization techniques, such as light beam induced current (LBIC) mapping, are valuable in such studies as they allow for immediate identification of recombination active regions where these defects lie.

LBIC mapping is a method based on measuring the locally induced short-circuit current at a particular wavelength for a given region of interest. By properly calibrating the laser probe power and correcting for reflection, it gives a map of the internal

of grain boundaries on the performance of the solar cell based on a few isolated grain boundaries. In this work, we demonstrate a quantitative approach in describing the collective impact of the grain boundaries based on their IQE values by combining LBIC, defect etching, and automated image recognition. This approach identifies the grain boundaries and their positions from defect-etched samples rather than from the IQE map itself. Contrary to methods that identify their positions using lifetime-dependent quantities such as photoluminescence (PL),^[21] defect etching shows all grain boundaries and not only those that are recombination active. Other works report the use of white light reflection (WLR) measurements on as-cut wafers to identify the grain boundaries.^[22] An even more precise method is microscopic imaging of polished and etched samples as presented in this work. Compared with PL imaging of as-grown wafers, our approach measures recombination on processed solar cells, making it more relevant to the final product. The method presented in this work does not rely on individual linescan contrast profiles of a few selected grain boundaries. Instead, all grain boundaries within the sampled region are considered. Furthermore, this method gives a quantity that describes the collective impact of grain boundaries together with a quantity that describes the combined impact of all other defects that may exist on the sample. The calculation of both quantities allows this method to be used to compare samples across different data sets unlike methods that rely on contrast profiles and therefore gives quantities that depend on the quality of intra-grain regions and therefore difficult to compare with different sample sets.

A. P. Pacho, Prof. M. Rinio
 Department of Engineering and Physics
 Karlstad University
 651 88 Karlstad, Sweden
 E-mail: aleopaolo.pacho@kau.se

 The ORCID identification number(s) for the author(s) of this article can be found under <https://doi.org/10.1002/pssa.202000229>.

© 2020 The Authors. Published by Wiley-VCH GmbH. This is an open access article under the terms of the Creative Commons Attribution License, which permits use, distribution and reproduction in any medium, provided the original work is properly cited.

DOI: 10.1002/pssa.202000229

2. Experimental Section

The distribution of IQE values at the positions of the grain boundaries were compared with the distribution of IQE values

at all other positions. The IQE values were determined using LBIC and the precise positions of the grain boundaries were identified using optical microscopy of defect-etched samples.

2.1. Solar Cell Samples and LBIC Measurements

Standard aluminum back surface field (Al-BSF) solar cells were fabricated from the bottom, middle, and top ingot positions of a high-performance multicrystalline silicon (HP mc-Si) brick. IQE maps at 826 nm wavelength were obtained using a custom-built LBIC system.^[23] The measurements were conducted at a spatial resolution of 50 μm with incident laser power of about 1.8 μW . Some regions containing structures that could be easily identified in an etched wafer were mapped at a resolution of 12.5 μm . These maps will aid in correlating the positions of the pixels of the IQE maps with those of the microscope images of the etched samples. A few IQE linescan profiles across grain

boundaries were also taken from these high-resolution IQE maps to get an idea of the spatial extent of the impact of the grain boundaries on the IQE. Reflection maps, also obtained using LBIC, were used to identify the positions of the contact fingers and busbars. In particular, pixels in the IQE maps where the total reflection exceeded 8% were excluded from the analysis.

2.2. Defect Etching and Microscopy

After the LBIC measurements, the cells were laser cut into 25 mm \times 25 mm sections. Four such samples from the region around the center of each cell were selected and further processed. The samples were then prepared for defect etching using a combination of chemical and mechanical polishing to ensure that the surfaces were free from scratches and subsurface deformations which can complicate the analysis. In particular, the samples were subsequently polished using diamond suspensions with particle sizes of 9, 3, and 1 μm . A final polishing was applied using a colloidal silica slurry and these were then subjected to a 1 min Secco etch^[24] to reveal the positions of the dislocations and grain boundaries. The samples were then imaged using an Olympus MX61A optical microscope equipped with a moveable stage and autofocus, at a resolution of about 0.34 $\mu\text{m pixel}^{-1}$, capturing an array of around 4800 images per sample. An overview image of a sample is shown in Figure 1.

2.3. Image Recognition and Correlation

The acquired array of images for each sample was analyzed using ImageJ.^[25–26] After performing shading correction, the images were binarized by assigning a grayscale threshold value that separated the background from the features. The grain boundaries were then identified using ImageJ's built-in particle analysis tool. The parameter circularity, defined as $\text{circularity} = 4\pi \times (\text{area} \times \text{perimeter}^{-2})$, has a value of 1.0 for a perfect circle and approaches 0 for increasingly elongated shapes. For the samples used in this work, objects with a circularity of less than 0.02 were regarded as grain boundaries. An example of a typical result for this process is shown in Figure 2. Note that the appropriate range of circularity values may depend on several factors such as the quality of the polishing and etching and the microscope resolution. The relative pixel coordinates of each pixel



Figure 1. Overview image of an etched sample. The brightness and contrast of the image shown here was adjusted after applying grayscale erosion to improve visibility.

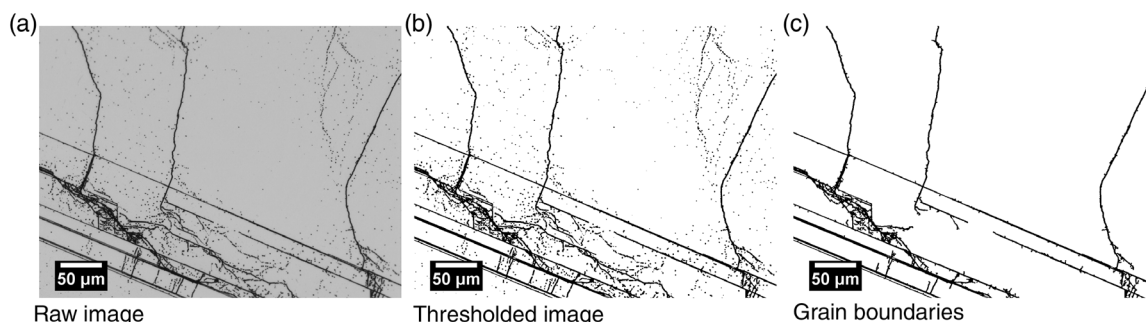


Figure 2. Segmentation of grain boundaries. a) A single raw microscopic image of the etched sample shown in Figure 1. The image in (b) is the result of binarizing (a) so that features appear as black pixels, whereas the background pixels are white. c) The result of detecting particles with circularities between 0 and 0.02 for this image.

detected as part of a grain boundary are translated into real microscope coordinates.

To be able to map the precise positions of the grain boundaries identified from the etched samples onto the IQE maps, high-resolution (12.5 μm) LBIC measurements were conducted on some regions which contain distinct features. The positions of these features were noted on the LBIC map and on the microscope image. The pair of positions were then used to translate the microscope coordinates of the grain boundaries into the LBIC map coordinates using a topographical correlation method.^[27] This procedure ensures that a subpixel correlation is obtained between the IQE maps and the microscope images, with about 4–10 μm spatial accuracy.

From the full 50 μm resolution IQE image of each cell, the regions that correspond to the etched samples were selected. As the actual effect of each grain boundary on the IQE may extend to its immediate surroundings, the grain boundary positions on the IQE maps were taken to be the pixels within a certain radius from the translated position coordinates, hereafter referred to as the masking width. In this work, masking widths of 50–500 μm were used to explore its effect on the calculations. Having identified the LBIC map coordinates of the grain boundaries in the samples, the IQE values at those positions were extracted and compared with the IQE at the other positions where defects other than grain boundaries, i.e., dislocations, may be present. This is shown in Figure 3.

3. Results and Discussions

To quantify the collective impact of grain boundaries on the IQE, we need to use a hypothetical average IQE that would serve as a reference value for comparison. The reference value must reflect a reliable estimate of the highest attainable average IQE for a sample. To this end, the mode of the IQE values of each cell was used as a threshold value for the corresponding samples. All pixels with IQE values greater than the threshold value were then selected, with the average IQE of these pixels taken to represent the highest possible average IQE for the particular cell. In this manner, the reference average IQE value is calculated from a subset of the IQE distribution instead of taking it from a single measurement, i.e., the highest measurement value,

which could just be an outlier. Positions where the measured IQE values are greater than the mode of the distribution, which is the measurement value that occurs most frequently in the sample, typically come from regions free of grain boundaries and dislocation clusters. Furthermore, the mode of the IQE distribution is a suitable threshold value as it is insensitive to outliers unlike the mean. The median value is less sensitive to outliers compared with the mean, but using it as the threshold value, i.e., taking the average of the upper 50% of the distribution, will give a more conservative estimate of the highest attainable average IQE. Another option is to select a small defect-free region on the sample and use the average IQE value in that region as the reference value. This can, however, be quite subjective as it is possible to choose different regions with different IQE values as shown in Figure 4. Using the mode as the threshold value and assuming that all points above the mode represent the highest attainable IQE values removes this subjectivity and ensures that the reference IQE average value remains reasonable. The reference average IQE values are listed in Table 1.

With this, the absolute reduction in IQE due to grain boundaries is calculated as the difference between 1) the average

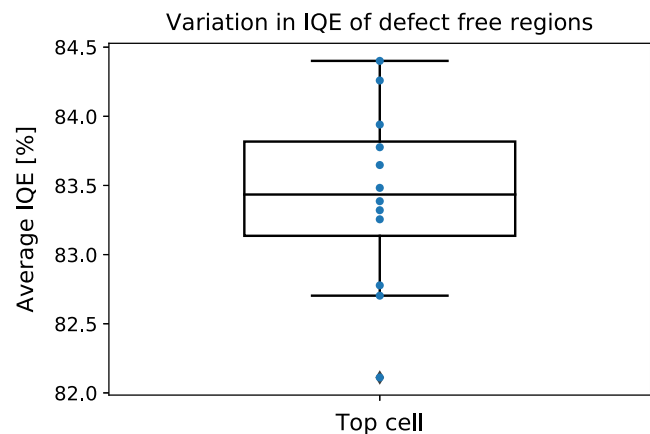


Figure 4. The average IQE of 12 different defect-free regions in the top cell. The relatively large variation in average IQE shows that selecting a defect-free region for the reference average IQE may lead to unrepeatable calculations and user bias.

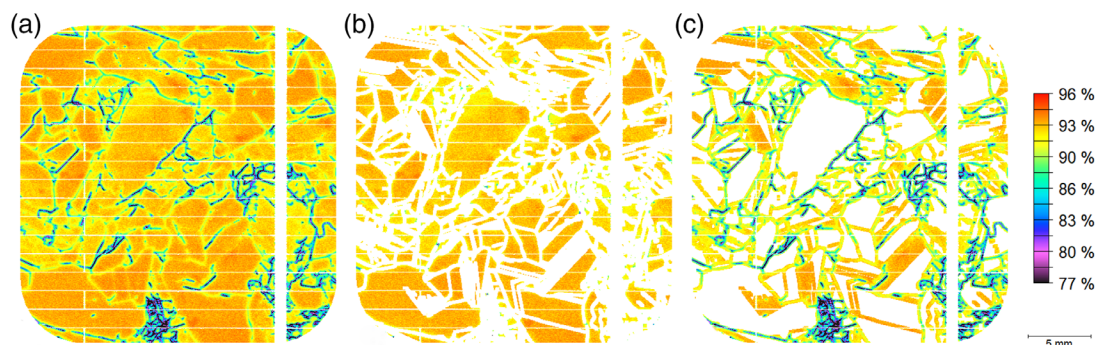


Figure 3. Typical result of mapping the grain boundary positions in an etched sample onto that sample's IQE map at 826 nm wavelength. The busbars and contact fingers are marked in white and are excluded from the calculations. a) The IQE map of the sample. b) The same map with the grain boundaries deleted, and (c) the IQE map at the positions of the grain boundaries. All three maps share the same IQE scale shown in the rightmost part of the figure.

Table 1. Reference average IQE values.

Ingot position	Threshold IQE [%]	Reference ave. IQE [%]
Bottom	92.00	92.65
Middle	92.80	93.23
Top	84.63	85.93

IQE if the pixels associated with grain boundaries had IQE values equal to the reference IQE average value and 2) the actual average IQE. The same calculation was applied for the pixels representing all other defects as summarized in Equation (1)

$$\text{IQE reduction (due to } G) = \frac{(N_G) \times (IQE_{\text{ref}} - IQE_G)}{\text{total number of pixels}} \quad (1)$$

where G is the group of pixels associated with either grain boundaries or all other regions, N_G is the number of pixels in group G , IQE_G is the average IQE of group G , and IQE_{ref} is the reference average IQE. A similar expression was used by Augarten et al., which utilized a reference PL signal either from a measurement of the sample without the shunt or from a homogenous non-shunted area of the sample to calculate the shunt current from PL images.^[28]

Any analysis derived from the grouping of IQE pixels such as the calculation of the reduction in IQE as shown in Equation (1) depend on the choice of masking width. Classifying a pixel in the IQE map as a grain boundary, in the context of this work, implies that the IQE value at that position is affected most greatly by the grain boundary in its immediate vicinity. Choosing an excessively large masking width is tantamount to assuming that there are no other defects within that distance from the grain boundaries that can significantly influence the IQE, and can therefore lead to an overestimation of the grain boundaries' impact on the IQE. In contrast, choosing the smallest possible width, i.e., 50 μm for our resolution, is clearly an underestimation as this would imply no lateral carrier diffusion. For our samples, 200 μm masking width is sufficient to incorporate the deteriorated IQE region surrounding grain boundaries. This is supported by Figure 5, which shows a few IQE linescans across isolated grain boundaries that appear to be recombination-active

in the IQE maps. We therefore report the results from 200 μm masking width but nevertheless present the results from the other masking widths as well.

The number of pixels associated with grain boundaries and all other pixels, together with their corresponding average IQE and the calculated absolute reduction in IQE as functions of the masking width are shown in Figure 6. The masking width value where the curves for the number of grain boundary pixels and number of all other pixels intersect is an indication of the average grain size of the cell and therefore varies with ingot position as expected.

The average IQE of each group increases as the masking width is increased from the minimum value. At the minimum value of the masking width, the positions in the immediate vicinity of each grain boundary are counted as nongrain boundary pixels. As the masking width is increased from this minimum value, the pixels in these deteriorated regions start to be correctly classified as grain boundary pixels and therefore excluded from the nongrain boundary group. The grain boundary group, which previously included only the minima of each grain boundary's corresponding linescan profile, now includes positions with relatively higher IQE values. The average IQE for both groups therefore increases as the masking width is widened from its minimum value. The behavior of the average IQE, as the masking width is further increased, may give a hint on the uniformity of the IQE values. In particular, the average IQE of the nongrain boundary groups for both the top and bottom cells eventually decreases while that of the middle cell appears to saturate in the range of masking widths considered. This may be attributed to a more uniform distribution of IQE values in the intra-grain regions of the middle cell compared with the intra-grain regions of the top and bottom cells. The behavior of the absolute reduction in IQE, as a function of masking width, reflects the combined trends of the number of pixels and average IQE of each group. Consequently, the absolute reduction in IQE due to grain boundaries for the middle cell appears to saturate and vary slowly with increasing masking width, whereas the corresponding absolute reduction in IQE for the top and bottom cells continues to increase in the range of masking widths considered.

The segmented IQE distributions are shown in Figure 7. In this figure, the pixels within 200 μm of the detected grain boundary positions are taken to be grain boundaries while all

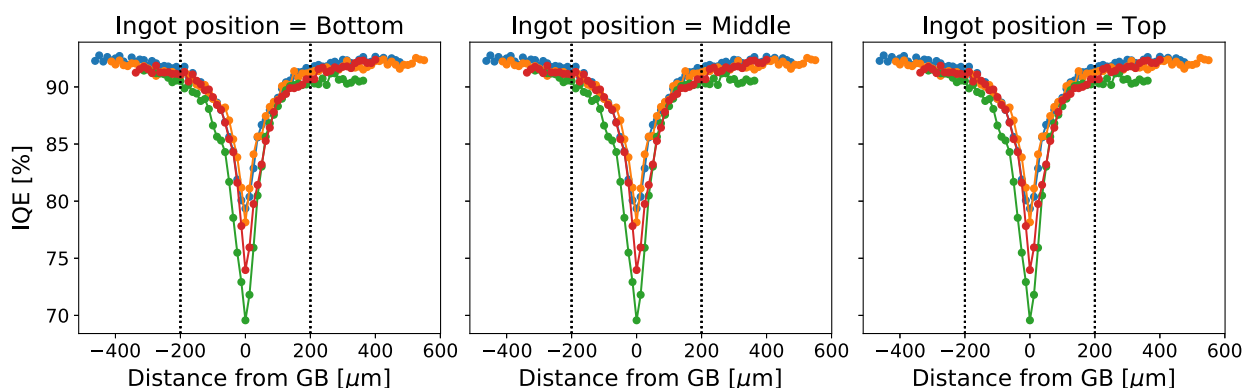


Figure 5. Typical IQE linescans across recombination-active grain boundaries. The grain boundary profiles were obtained from the 12.5 μm spatial resolution IQE maps of the corresponding cell.

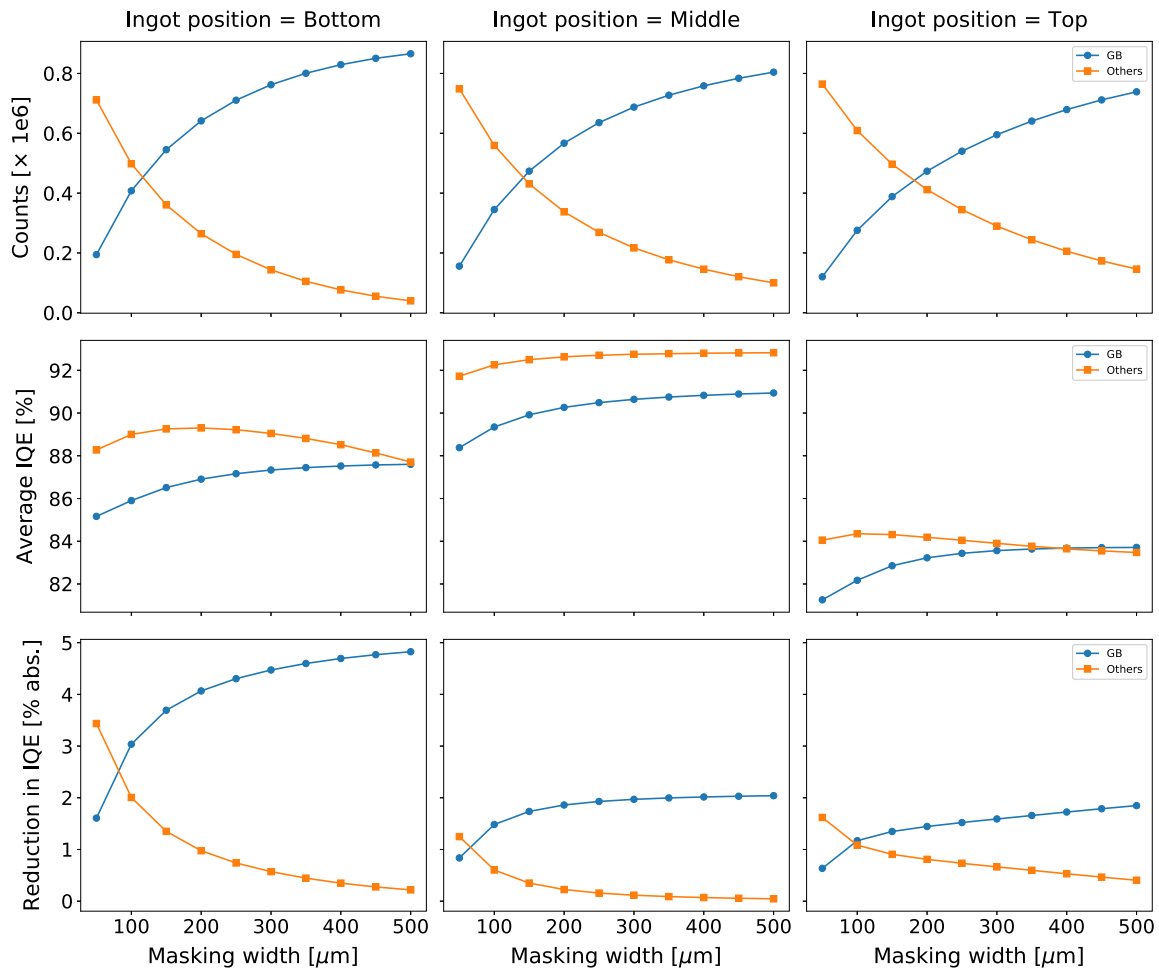


Figure 6. Number of pixels, average IQE, and absolute reduction in average IQE as functions of the masking width. The groups labeled “GB” include pixels identified as grain boundaries, whereas all other pixels are included in the groups labeled “Others” for each corresponding masking width.

other positions are included in the group labeled “Others”. With the scaling performed for each cell, the width of each shape at each IQE value is a representation of the number of observations for that IQE value. The figure shows that nongrain boundary pixels of the middle cell have a tighter distribution compared with the nongrain boundary pixels of the top and bottom cells. This supports the earlier observation that the intra-grain regions of the middle cell have a more uniform distribution of IQE values compared with the corresponding pixels of the top and bottom cells.

Also shown inside each half violin figure are the quartiles of the distribution. In the bottom and middle cells, the median of all grain boundary pixels are lower than the median of the corresponding distribution for all other pixels. For these cells, even the third quartile is lower than the median of the corresponding distribution for all other pixels. This further supports the observation that grain boundaries generally have lower IQE values compared with all other positions for these cells. Furthermore, no bimodality is observed in the grain boundary distributions despite the fact that no distinction was made between recombination active and inactive grain boundaries. Nevertheless, we observe a wider spread in the IQE distributions

for the grain boundaries compared with the positions without grain boundaries, especially in the bottom and middle cells. For the top cell, the difference between the distributions of grain boundary and nongrain boundary pixels is not as striking. The low average IQE for this cell may not be directly attributed to the presence of grain boundaries.

The absolute reduction in average IQE calculated from a masking width of 200 μm is summarized in **Figure 8**. In this figure, the group labeled “GB” again represents the pixels within 200 μm of the detected grain boundaries, whereas the group labeled “Others” represents measurements from all other positions. For all three ingot positions considered, grain boundaries gave a greater absolute reduction in the average IQE of the corresponding cell. The impact of grain boundaries decreases with increasing ingot height. The observation that the cells from different ingot positions show different values for the absolute reduction in IQE due to grain boundaries show that cells with different grain structures are affected by grain boundaries in varying degrees. For the middle cell which had the greatest average IQE among the cells considered, the reduction due to nongrain boundaries was lowest compared with the other cells. The reduction due to grain boundaries, however, remain

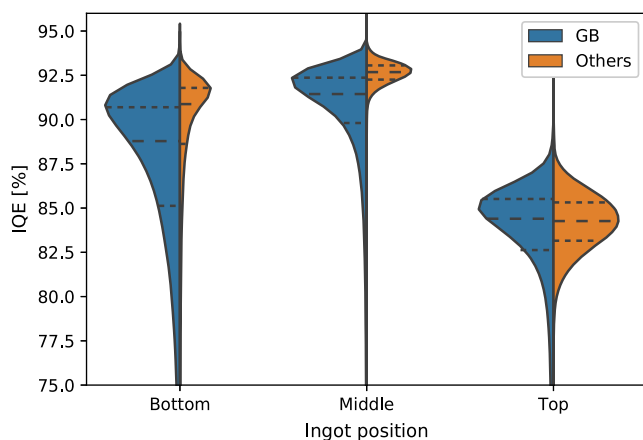


Figure 7. Distribution of segmented IQE values using a masking width of 200 μm . The width of each shape represents the number of observations for the corresponding IQE value, with the scaling performed for each cell. The dashed lines inside each figure represent the quartiles of the corresponding distribution. The groups labeled “GB” are comprised of pixels within 200 μm of the detected grain boundary positions, whereas all other positions are included in the groups labeled “Others”.

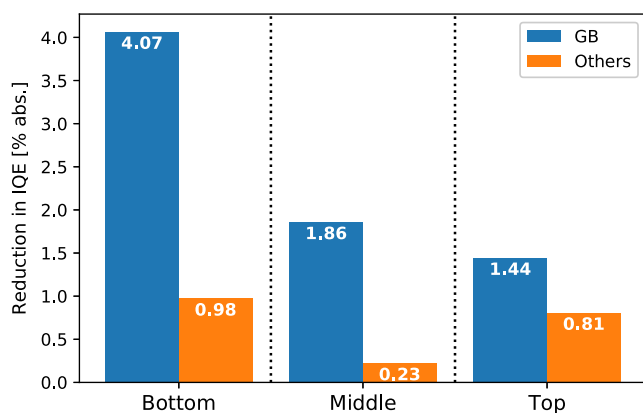


Figure 8. Absolute reduction in the average IQE using a 200 μm masking width. The group labeled “GB” represents the pixels within 200 μm of the detected grain boundaries, whereas the group labeled “Others” represents all other pixels.

substantial. This implies that while the quality of the wafer is optimized at the middle ingot positions, the presence of grain boundaries limit its IQE. The impact of grain boundaries and the combined effect of all other possible defects on the top cell are comparable. The relatively lower IQE for this cell, therefore, may not be attributed solely to the recombination activity of grain boundaries but also to other phenomena such as accumulation of impurities via impurity segregation during ingot growth.

The absolute reduction in average IQE, as calculated from Equation (1) and summarized in Figure 8, directly address the question of how much the grain boundaries actually impact the IQE of the cell. This quantity describes the amount of reduction in the IQE that can possibly be attributed to the presence of grain boundaries. Alternatively, this quantity can be thought of as the greatest gain in average IQE that can be reasonably expected if the grain boundaries did not exist in the sample, or if they

were completely passivated such that they do not contribute to current losses. The fact that this quantity was calculated relative to a reference value specific to a particular cell, as previously discussed, means that the calculation incorporates all factors that may affect the resulting performance of the cell and makes no assumption on any physical property other than the greatest plausible average IQE which was statistically determined.

It is important to emphasize that the absolute reduction in IQE due to grain boundaries measured here depends on the solar cell architecture. It will be larger for improved cell structures that better suppress minority carrier recombination at the rear surface and the rear contacts, where the electrical properties are more sensitive to the bulk material quality.^[29–30] With the trend in cell technologies going from standard Al-BSF to PERC processes^[1] and will likely proceed towards better passivating contacts such as TOPCon,^[31] these IQE reductions from bulk defects will become even more relevant.

4. Conclusion

A method to quantify the collective impact of grain boundaries on the IQE of mc-Si solar cells has been presented in this work. In comparison with the combined effect of all other crystal defects that may be present at positions of at least 200 μm away from detected grain boundaries, grain boundaries proved to be more detrimental to the IQE at 826 nm in our samples. The reduction in the IQE at 826 nm due to grain boundaries was largest for the cell from the bottom of the ingot. On the sample from the middle of the ingot, which exhibited the greatest measured average IQE, it was seen that while the reduction in IQE due to all other defects was minimized (0.23% abs.), the detrimental effect of grain boundaries remains significant (1.86% abs.).

Amid the fairly recent trend of utilizing crystal growth methods that produce smaller grain sizes^[32] and therefore more grain boundaries, the results suggest that grain boundaries as a group can significantly diminish the electrical performance of a cell and must therefore be taken into consideration in the development of crystallization techniques. The method described in this work can be used to further compare the impact of grain boundaries on the IQE of cells from different crystallization methods that produce different grain structures.

Acknowledgements

This work was supported by the Solar-Era.Net project “HighCast” via the Swedish Energy Agency under project number 40184-1, the project “Advanced analysis of industrial silicon wafers for solar cells” via J. Gust. Richert stiftelse, and the project “Solar Värmland” via Region Värmland and Tillväxtverket under project number 20201237. The authors also acknowledge Dr. Stephan Riepe and Dr. Adam Hess of Fraunhofer ISE for providing the as-grown Si wafers used in this work. The authors would also like to thank Prof. Jens Bergström for valuable comments on the manuscript.

Conflict of Interest

The authors declare no conflict of interest.

Keywords

grain boundaries, internal quantum efficiency, light beam induced current, multicrystalline silicon, solar cells

Received: April 17, 2020

Revised: June 29, 2020

Published online: August 2, 2020

- [1] ITRPV, *International Technology Roadmap for Photovoltaic – Results 2018 Including Maturity Report 2019*, ITRPV, Frankfurt am Main **2019**.
- [2] A. Stoffers, O. Cojocaru-Miredin, W. Seifert, S. Zaeffere, S. Riepe, D. Raabe, *Prog. Photovoltaics* **2015**, 23, 1742.
- [3] J. Chen, T. Sekiguchi, D. Yang, F. Yin, K. Kido, S. Tsurekawa, *J. Appl. Phys.* **2004**, 96, 5490.
- [4] T. Buonassisi, A. A. Istratov, M. D. Pickett, M. A. Marcus, T. F. Ciszek, E. R. Weber, *Appl. Phys. Lett.* **2006**, 89, 042102.
- [5] H. C. Sio, S. P. Phang, D. Macdonald, *Sol. RRL* **2017**, 1, 1600014.
- [6] H. C. Sio, T. Trupke, D. Macdonald, *J. Appl. Phys.* **2014**, 116, 244905.
- [7] M. Di Sabatino, G. Stokkan, *Phys. Status Solidi A* **2013**, 210, 641.
- [8] G. Stokkan, S. Riepe, O. Lohne, W. Warta, *J. Appl. Phys.* **2007**, 101, 053515.
- [9] C. Donolato, *J. Appl. Phys.* **1998**, 84, 2656.
- [10] M. Rinio, S. Peters, M. Werner, A. Lawrenz, H. J. Möller, *Solid State Phenom.* **2002**, 82–84, 701.
- [11] K. Adamczyk, R. Sondenå, C. C. You, G. Stokkan, J. Lindroos, M. Rinio, M. Di Sabatino, *Phys. Status Solidi A* **2018**, 215, 1700493.
- [12] S. Castellanos, M. Kivambe, J. Hofstetter, M. Rinio, B. Lai, T. Buonassisi, *J. Appl. Phys.* **2014**, 115, 183511.
- [13] M. Rinio, A. Yodyungyong, S. Keipert-Colberg, D. Borchert, A. Montesdeoca-Santana, *Phys. Status Solidi A* **2011**, 208, 760.
- [14] K. Adamczyk, R. Sondenå, G. Stokkan, E. Looney, M. Jensen, B. Lai, M. Rinio, M. Di Sabatino, *J. Appl. Phys.* **2018**, 123, 055705.
- [15] J. Chen, T. Sekiguchi, *Jpn. J. Appl. Phys.* **2007**, 46, 6489.
- [16] C. Donolato, *Rev. Sci. Instrum.* **1983**, 54, 1005.
- [17] C. Donolato, *J. Appl. Phys.* **1983**, 54, 1314.
- [18] G. Micard, G. Hahn, A. Zuschlag, S. Seren, B. Terheiden, *J. Appl. Phys.* **2010**, 108, 034516.
- [19] R. Corkish, T. Puzzer, A. B. Sproul, K. L. Luke, *J. Appl. Phys.* **1998**, 84, 5473.
- [20] J. D. Zook, *Appl. Phys. Lett.* **1980**, 37, 223.
- [21] H. C. Sio, S. P. Phang, A. Fell, H. Wang, P. Zheng, D. Chen, X. Zhang, T. Zhang, Q. Wang, H. Jin, D. Macdonald, *Sol. Energy Mater. Sol. Cells* **2019**, 201, 110059.
- [22] T. Strauch, M. Demant, P. Krenckel, S. Riepe, S. Rein, *J. Cryst. Growth* **2016**, 454, 147.
- [23] M. Rinio, H. J. Möller, M. Werner, *Solid State Phenom.* **1998**, 63–64, 115.
- [24] F. Secco d'Aragona, *J. Electrochem. Soc.* **1972**, 119, 948.
- [25] J. Schindelin, I. Arganda-Carreras, E. Frise, V. Kaynig, M. Longair, T. Pietzch, S. Preibisch, C. Rueden, S. Saalfeld, B. Schmid, J. Y. Tinevez, D. J. White, V. Hartenstein, K. Eliceiri, P. Tomancak, A. Cardona, *Nat. Methods* **2012**, 9, 676.
- [26] C. A. Schneider, W. S. Rasband, K. W. Eliceiri, *Nat. Methods* **2012**, 9, 671.
- [27] M. Rinio, A. Hauser, H. J. Möller, presented at 3rd World Conf. on Photovoltaic Energy Conversion, IEEE, Osaka, Japan **2003**.
- [28] Y. Augarten, T. Trupke, M. Lenio, J. Bauer, J. Weber, M. Juhl, M. Kasemann, O. Breitenstein, *Prog. Photovoltaics* **2013**, 21, 933.
- [29] H. C. Sio, S. P. Phang, P. Zheng, Q. Wang, W. Chen, H. Jin, D. Macdonald, *Jpn. J. Appl. Phys.* **2017**, 56, 08MB16.
- [30] G. Coletti, *Prog. Photovoltaics* **2013**, 21, 1163.
- [31] F. Feldmann, M. Bivour, C. Reichel, H. Steinkemper, M. Hermle, S. Glunz, *Sol. Energy Mater. Sol. Cells* **2014**, 131, 46.
- [32] C. Lan, A. Lan, C. Yang, H. Hsu, M. Yang, A. Yu, B. Hsu, W. Hsu, A. Yang, *J. Cryst. Growth* **2017**, 468, 17.